Heliyon 8 (2022) e09626

Contents lists available at ScienceDirect

Heliyon

journal homepage: www.cell.com/heliyon

Research article

Techniques for bone assessment and characterization: porcine hard palate case study

A. Cañas-Gutiérrez [a,*], D. Arboleda-Toro [b], T. Monsalve-Vargas [b], C. Castro-Herazo [a], J.M. Meza-Meza [c]

[a] Grupo de Investigación Sobre Nuevos Materiales (GINUMA) School of Engineering, Universidad Pontificia Bolivariana, Circular 1 # 70-01, Medellín, Colombia
[b] Grupo de Estudios BioSociales Del Cuerpo, School of Dentistry, Universidad de Antioquia, Calle 64 No. 52-59, Medellín, Colombia
[c] Design of Advanced Composite Structures – DADCOMP, Universidad Nacional de Colombia, Carrera 79 No 75 A-53, Medellín, Colombia

ARTICLE INFO

Keywords:
Bone
Hard palate
The palatine process of maxilla
Hydroxyapatite
Characterization techniques

ABSTRACT

The hard palate plate has an important structural function that separates the nasal cavity and the nasopharynx. Incomplete regeneration of palatal fistulae in children with a cleft palate deformity after primary palatoplasty is a relatively common complication. To date, the information about the physicochemical bone features of this region is deficient, due to the low availability of human samples. Swine and human bone share anatomical similarities. Specifically, pig bones are widely used as experimental animal models in dental, orthopedic, or surgical techniques. The aim of this study was to show different techniques to evaluate and characterize alternative properties of pig hard palate bone, compared to commercial hydroxyapatite, one of the most used biomaterials for bone tissue regeneration. Chemical analyses by Energy dispersive spectroscopy (EDS) and X-ray fluorescence (XRF) showed calcium and phosphate ions as the main constituents of bone, while magnesium, iron, sodium, potassium, and zinc ions were minor constituents. The calcium phosphate molar ratio (Ca/P) in the bone was low (1.1 ± 0.2) due to the very young specimen sample used. The FTIR spectrum shows the presence of phosphates ions (PO_4^{3-}) and the main characteristics of collagen type I. The XRD results showed that the hard palate bone has a mixture of calcium, octacalcium dihydrogen phosphate (OCP), and apatite, where OCP is the predominant phase. Besides, this research demonstrated that the young bone has low crystallinity and small crystal size compared with commercial hydroxyapatite (HA). The palatine process of maxilla density and porosity data reported, suggest that the palate bone is getting closer to the compact bone with a $52.78 \pm 2.91\%$ porosity and their mechanical properties depend on the preparation conditions and the area of the bone analyzed.

1. Introduction

The hard palate is an anatomical structure that has not been fully investigated; it forms the upper part of the oral cavity and separates the mouth from the nasal cavity and nasopharynx (Shah and Garritano, 2015). Current studies associated with the upper jaw of mammals are focused mainly on their growth and development (Melsen, 1975; Montenegro and Rojas, 2005; Sun et al., 2017; Tenorio Estrada, 2017) and, on the analysis of the characteristics of the alveolar bone and its repair (Huang et al., 2015; Watson et al., 2018). To date, however, no studies have correlated the structural and chemical characteristics of the bone in the hard palate with the bone grafts used in current treatments to understand the possible causes of their failures. Moreover, there are no reports on the microstructure and chemical composition of the bone palate area. Therefore, it is necessary to carry out a study on the tissue of interest to understand its characteristics.

In general, bone is a complex tissue composed of an organic and an inorganic phase. The mineral phase in bone performs two major functions: as a structural material and as an ion reservoir. In contrast, the organic phase contains cells and extracellular matrix constituents, mainly type I collagen fibrils that vary in relative proportions according to the age and health of the organism. Both phases are complex structures, where the basic building blocks are the plate-like HA nanocrystals deposited within the collagen fibrils (Glimcher, 1998). Currently, various characterization techniques are used to relate their 3D structure, composition, and mechanical properties. Areas like Osteology (Boyde and Jones, 1998), Forensics (Shah et al., 2019), Archeology (Reznikov et al., 2018), Biomaterials and Tissue engineering (Matassi et al., 2011)

* Corresponding author.
E-mail address: ana.canas@upb.edu.co (A. Cañas-Gutiérrez).

https://doi.org/10.1016/j.heliyon.2022.e09626
Received 25 October 2021; Received in revised form 21 January 2022; Accepted 27 May 2022

are exploiting the advances in those fields. Several studies have studied specific characteristics of the bone like the nanostructure (Davies et al., 2014), microarchitecture (Georgiadis et al., 2016; Pazzaglia et al., 2012), mechanical properties (Gibson et al., 2006; Hoffler, 2005; Wu et al., 2012), chemical composition (Boskey and Mendelsohn, 2005), biochemical markers (Starup-Linde et al., 2016), crystallinity (Querido et al., 2013), density (Dumont, 2010), and bone quality (Aerssens et al., 1998; Malluche et al., 2012). Although various techniques were described, most of the studies are focused on only one technique.

Combining various techniques provides precise information on the characteristics of the bone. For example, bone morphology can be studied by polarized light microscopy (PLM) and scanning electron microscopy (SEM). These techniques can be complemented with mechanical and chemical analyses as the structure of this tissue depends on the maturation and aging processes.

Among the chemical analyzes are Energy dispersive X-ray spectroscopy (EDS) and X-ray fluorescence (XRF). Both methods show its mineral content (Bush et al., 2008). When these analyzes are done in conjunction with the Fourier Transform Infrared Spectroscopy (FTIR) in the attenuated total reflection (ATR) mode it is possible to identify the presence of functional groups associated with the bone mineral. When X-ray diffraction (XRD) analysis is added, the crystalline phases of the bones can additionally be obtained (Tadano and Giri, 2011). As a complement to chemical analysis, thermogravimetric analysis (TGA) in bone gives the relative proportions of the bone matrix components. TGA analyses are important not only to determine the organic and water content in the samples (Figueiredo et al., 2011), but also in helping to analyze the EDS, XRF, FTIR and mechanical outcomes.

Finally, choosing the specimen or bone sample to be analyzed will depend on the type of study and the characteristics to be evaluated. Animal models are widely used to study different aspects of bone tissue such as bone loss, aging, fracture healing, calcium homeostasis, and the effects of drug treatment. However, differences between species in bone composition, density, and quality make it difficult to have an ideal model that can be used for different purposes in bone research. The number of animals used, age, breed, sex, and anatomical site introduce bias that might influence the results. Some authors have shown that properties of pig and dog bones resemble human bones (Aerssens et al., 1998). Pigs are extensively used as animal models for dental, orthopedic, and surgical technique research (Pyszko et al., 2013). These animals provide an excellent initial model for human bone study because pigs are diurnal omnivores like humans and share some anatomical similarities to human bone (Inui et al., 2004).

Therefore, the aim of this paper is to use different physicochemical techniques to characterize porcine palatal bones. The chemical characteristics and density of the porcine bone palate were compared with commercial hydroxyapatite, one of the most used biomaterials for bone tissue regeneration. Also included is a short description of the relevant theoretical aspects of commonly used techniques, stressing their advantages and disadvantages.

2. Materials and methods

2.1. Raw materials

The palate bones used in this study are waste products of the local meat industry, supplied to the Universidad UPB. A total of 10 Yorkshire swine palate bones were characterized. For morphological analysis, the starting sample used in this study was the hard palate of a 13-week-old pig obtained from the butchery 24 h after slaughter. It was kept refrigerated at 4 °C but never frozen. The soft tissue was removed with a scalpel and the bone marrow was washed with hot water at 80 °C. Five 5 × 5 × 0.4 mm samples were extracted from the central region of the maxillary palatine process (PPM) with the low-speed motor (Marathon 3, Korea 35000 rpm) (see Figure 1). The cleaned PPM parts were dried at 60 °C for 24 h and then stored in a desiccator. Some of the results were compared with a commercial hydroxyapatite powder from Strem Chemicals.

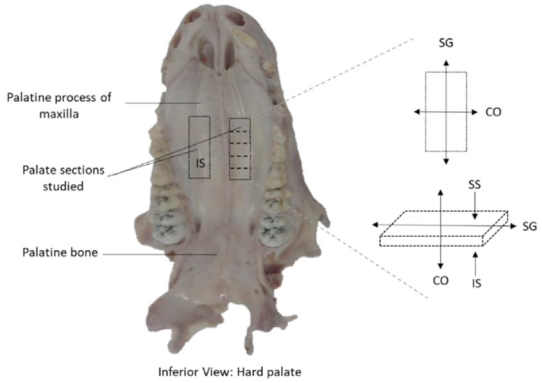

Figure 1. Inferior view of pig hard palate. The pig palate section evaluated was palatine process of maxilla. The analyzed sections were superior (SS) and inferior surface (IS), sagittal (SG) and coronal (CO) section for morphology, chemical composition, and mechanical properties.

2.2. Physical characterization

2.2.1. Morphology and microstructure

Figure 1 shows the different palatal processes analyzed from the central maxillary sections (PPM): sections of the upper (SS) and lower (IS), sagittal (SG) and coronal (CO) surfaces. Morphology and microstructure were studied by simple Polarized Light Microscopy (PLM) in a Nikon Eclipse LV100ND microscope and by Scanning Electron Microscopy (SEM) equipped with an energy dispersive X-ray spectroscopy (EDS) system, using a JEOL JSM 6490 LV in high vacuum mode. The surface and cross-section of samples were sputter-coated with gold.

The samples for optical microscopy PLM were embedded in epoxy resin and mechanically polished following metallographic standard procedures including emery papers (P800, P1200, and P2400 constantly irrigated with deionized water) and a last polishing step with a 0.3 μm diamond suspension. Finally, the samples were ultrasonically cleaned in a deionized water bath.

2.2.2. Density and porosity

To measure bone tissue density and bone porosity, five samples of PPM (see Figure 1) were completely dried at 60 °C for 24 h before the analysis. Real density or bone mineral density (ρr) was measured by helium displacement using a gas pycnometer (Micromeritics AccuPyc II 1340). The number of purges and the number of cycles were 100 for each sample with an equilibration rate of 0.0050 psig/min.

Apparent density (ρ_a) and porosity measurements were determined according to the ISO 10545-3 (ISO 2018) and ASTM C20 − 00 standard (ASTM C20-00, 2015). The initial weight of the samples was obtained. Then, the samples were saturated with distilled water and weighed again. The apparent density (ρ_a) and apparent porosity (P_a) of the PPM parts were calculated using Eqs. (1), (2), and (3):

$$P_a\,(\%) = \left[\frac{W-D}{V}\right] x100 \tag{1}$$

$$\rho_a\left(\frac{g}{cm^3}\right) = D\Big/V \tag{2}$$

$$V\left(cm^3\right) = W - S \tag{3}$$

Where W is the saturated weight, D is the dry weight, S is the suspended weight and V is the exterior geometrical volume. This assumes that 1 cm^3 of water weighs 1 g. Three measurements were made for each sample. The total porosity (*Pt*) and pore interconnectivity (*pi*) of the palate bone were then calculated using Eqs. (4) and (5) (Liu and Miao 2005):

$$Pt\ (\%) = \left(1 - \frac{\rho_a}{\rho_r}\right) * 100 \quad (4)$$

$$pi\ (\%) = P_a / Pt \quad (5)$$

Finally, the ratio of bone material volume over tissue volume (BV/TV) was calculated using Eq. (6) (Zioupos et al., 2008):

$$\frac{BV}{TV} = \frac{\rho_a}{\rho_r} \quad (6)$$

2.2.3. Mechanical characterization

Mechanical behavior was studied using a Nano indenter IBIS Authority- Fischer Cripps labs. PPM polished samples were glued to a steel slab using a rigid crystal bond resin. SS, IS, CO and SG surfaces were investigated. Ten indentations per selected area were made in a matrix arrangement in each section. The distance between indentation was 10 microns to avoid the influence of the cracks and densification of the material. The nanoindentation experiments were carried out with a fully calibrated area function of a Berkovich indenter with a tip radius of approximately 150 nm. The specimen was loaded at a constant loading rate to a maximum load of 3 mN. The load was maintained during 15 s to prevent creep effects during unloading. Testing in all cases were performed at room temperature and 40 % of humidity, thermal drift effects were minimized to allow the system to stabilize the temperature during at least 1 h after the samples were inserted in the table of the nanoindenter equipment. Young's module, E, and hardness, H, were calculated from the load–displacement curves using the Oliver–Pharr method (Oliver and Pharr, 1992) using a Poisson's ratio of 0.3 (Guidoni et al., 2010; Hoffler, 2005).

2.3. Chemical analyses

2.3.1. Thermal analysis

The relative proportions of the components of the bone matrix as mineral and organic material were obtained by thermogravimetric analysis (TGA). A total of 11 mg of the PPM dried powder and the HA samples were weighed and heated in a nitrogen atmosphere from 30 to 800 °C with a heating rate of 10 °C/min in a Mettler Toledo TGA/SDTA 851E thermogravimetric analyzer.

2.3.2. Elemental analyses

To determine the chemical concentration and distribution of the Ca and P of PPM, the four sections (SS, IS, CO and SG) were analyzed with elemental X-ray maps by EDS. The surfaces were covered with graphite, and the C and O elements were removed from quantification. Also, one gram of PPM powder was analyzed by X-ray fluorescence (XRF) in an ARLTM Optim's WDXDR Spectrometer Thermo Scientific in a helium atmosphere. To perform the XRF analysis, the percentage of residues of the materials evaluated by the TGA was considered to make the respective corrections of organic phase content.

2.3.3. Fourier transform infrared spectroscopy (FTIR)

FTIR - ATR mode was used to identify the presence of functional groups associated with the mineral and organic phases in PPM and HA samples. The spectrums were obtained in a PerkinElmer Spectrometer – model Spectrum One detector DTGS, and they were registered between 4000-400 cm^{-1} region using 64 scans and a spectral resolution of 6 cm^{-1}. Six measurements were performed in different places of each PPM section and HA.

2.3.4. X-ray diffraction (XRD)

XRD patterns were used to determine the mineral phases present in PPM sample and the apparent crystal size of the mineralized portion. The investigation was performed using a Rigaku diffractometer with a copper (Cu) source. The diffraction patterns were obtained for $5^\circ < 2\theta < 50^\circ$ with a step size of 0.02°. The data were analyzed using HighScore Plus Release: Version 3.0d software to identify the crystalline phases (in the mineralized portion of the pig bone) with Search and Match functions (Aguiar et al., 2018; Hafsteinsdó ttir et al., 2013). The Scherrer Eq. (7) was used to estimate the apparent crystal size (τ):

$$\tau = K\lambda / \beta cos\theta \quad (7)$$

Where K is a shape factor (a value of 0.94 was chosen for the elongated crystallites of bones) (Legros et al., 1987), λ is the wavelength of the X-rays (0.15406 nm), θ is the Bragg's angle and β is the full width at half maximum (FWHM) of the peak intensity corresponding to the (0 0 2) reflection (Figueiredo et al., 2010; Aguiar et al., 2018).

2.3.5. Statistical analyses

All the statistical analyses were carried out using the Statgraphics Centurion Version 2007. The data were analyzed by analysis of variance (ANOVA) and the differences between the means determined by the LSD Fisher multiple comparison test. For data of test pairs that did not meet the assumptions for ANOVA, were performed a Kruskal–Wallis (K–W) test. A value of $p \leq 0.05$ was considered statistically significant.

3. Results and discussion

3.1. Physical characterization

The purpose of characterizing the physical properties of bone is to know its microstructure and how they are directly related with other properties such as mechanical and density.

3.1.1. Morphology and microstructure

Figure 2 shows the surface resulting from the removal of bone cells from the surface of the bone matrix in the four PPM sections. Figures 2a-d show the microscopic structure through Polarized light microscopy (PLM). These images show characteristics of compact bone in all four sections with numerous spots called lacunas (black circles marked with yellow arrows) (Georgiadis et al., 2016). The concentric layers around the osteons were observed only in SS and IS (marked with blue lines in Figure 2 a and b). In these sections, it is possible to observe a pattern of concentric laminar structures (secondary osteons) composed of rings of concentric lamellae around each pore as reported by other studies (Martiniaková et al., 2008). These results are associated with immature bone, due to the early stages of puberty in which the pig has been slaughtered (Inui et al., 2004). Comparing the age of the pig studied with that of a human, it can be said that anatomically the age of the pig corresponds to a human between 13 and 16 years of age, which corresponds to the stage of puberty (Litten-Brown et al., 2010). Despite the porosity observed in CO and SG sections (see Figure 2-c and d), the trabecular bone structure was not present in the central PPM region. These results suggest that the structure of the palate bone is not similar to a flat bone, and as will be seen later, density measurements suggest a similarity with compact bone. This has not been reported in the literature yet.

The SEM images of the four bone sections obtained in this investigation can be seen in Figure 2 e-l. Figures 2e-i and 2f-j show the bone surface of the SS and IS sections respectively. Both surfaces show canals with a diameter between 200–300 μm. Each canal is associated with the organization of the bone at a microstructural level through the development of the Haversian systems and the concentric laminar structures formation that grow around the canals and take shape during the process of bone maturation (Pazzaglia et al., 2012).

In the CO and SG sections, the directions of the Haversian systems and the canals that cross the hard palate in the SS to SI direction can be observed (see Figures 2g and h). There are different structures in the process of formation between the SS and SI surfaces associated with the collagen fiber pattern. The SS surface showed a small sharp structure, whereas the IS surface showed the directional structures associated with

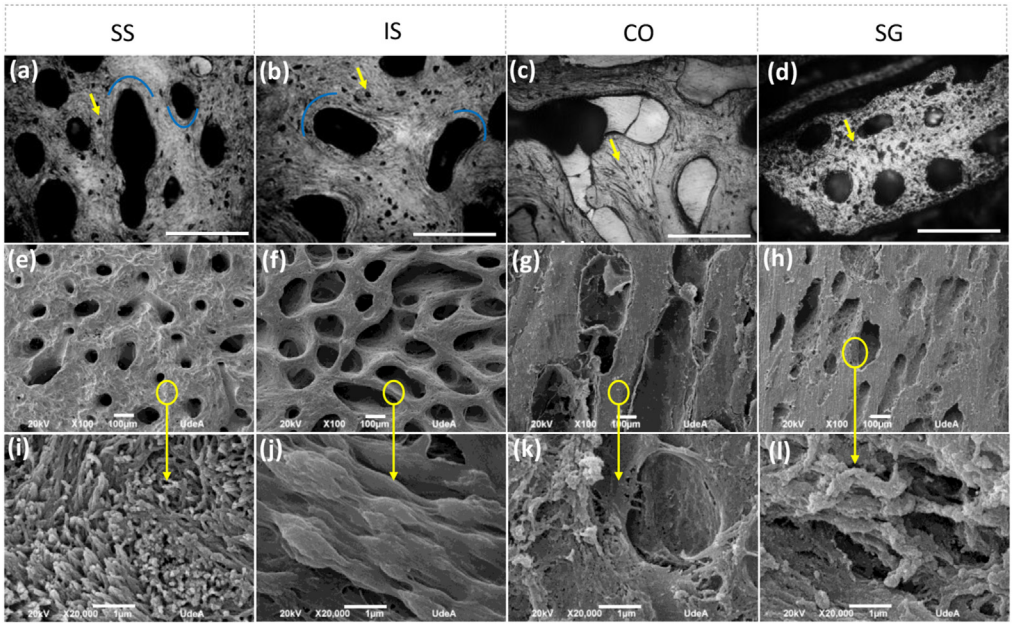

Figure 2. PPM morphology in the four sections (SS, IS, CO and SG) of the hard palate bone of the pig. Images a to c were taken from a polished sample using a Polarized light microscopy and the scale bar length is 200 μm. Images e to h (100 x scale bar length is 100 μm) and images to l (20000 x scale bar length is 1 μm) were taken from as fractured sample using a SEM.

the mineralization process. This could be because these surfaces were submitted to different mechanical requests (during feed) that change the roughness of the bone surface. The constant pressure of the tongue against the palate affects the directional structures associated with the mineralization process (see Figures 2i and j).

Figures 3a-d show the bone surface of the SS section. Inside the canals, the concentric orientation that forms the mineralized fiber is evident; this is associated with the process of bone maturation. The non-collagenous mineralized portion of the matrix shown in Figures 3a and d reveals the pattern of collagen fibers in specific directions of the mineralization process with an architecture of concentric laminar structures of secondary osteons (Haversian systems), composed of rings of concentric lamellae around each canal (Tadano and Giri, 2011) (see white lines). This section is similar to transverse sections of human cortical bone as reported by Pazzaglia et al. (2012). Comparing the results of PLM and SEM, PLM is a simple and inexpensive method that allowed us to observe the tissue structure (lacunae, osteons, and lamellae) (Bromage et al., 2003; Pyszko et al., 2013). While SEM allowed

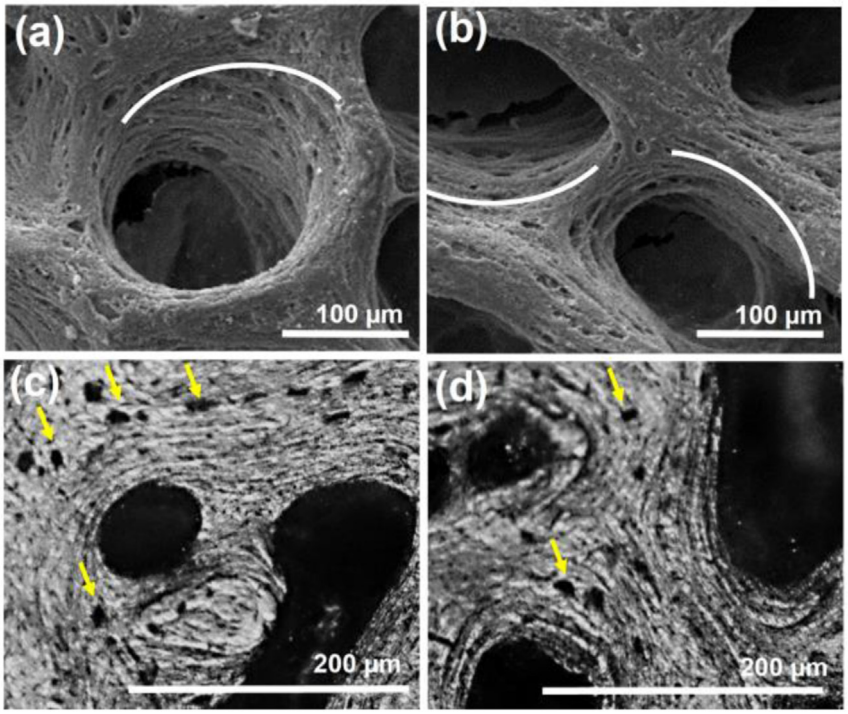

Figure 3. Microstructural analysis of the upper bone surface (SS) of the pig hard palate bone. a) and b) SEM images showing the concentric direction of the bone mineralization process marked with white lines. c) and d) PLM images where the lacunas are observed (small black dots marked with yellow arrows).

Table 1. Density and porosity of PPM.

ρ_r (g/cm^3)	*Pa* (%)	ρ_a (g/cm^3)	*Pt* (%)	BV/TV
2.105 ± 0.126	53.365 ± 3.926	0.993 ± 0.097	52.785 ± 2.913	0.472

* Significant difference ($P < 0.05$). Data were analyzed by one way ANOVA. Mean ± S.D., n = 5.

us to observe the textural patterns associated with cellular activity on the bone surface associated with the maturation process (Boyde and Hobdell, 1968). Therefore, these two techniques are complementary.

3.1.2. Density and porosity

The results of the density and porosity are presented in Table 1. To measure the apparent density and real density, in this research we make a correlation between the ASTM C20-00 (2015) standard, and the helium pycnometer technique. All five samples were taken from the palatine process to the maxilla region (see Figure 1) without the median palatine suture region that involves the nasal crest of the maxilla, a highly porous region. The results showed that the real density is higher compared with the apparent density and they also showed a statistically significant difference ($P < 0.05$). The bone density and porosity data suggest that the palate bone is resemblant to compact bone (Mbarki, 2017), and as also shown by SEM and PLM analyses, the structure of the palate bone section is not composed of trabecular or cancellous bone tissue (Gracco et al., 2008). This is consistent since, the difference between the two densities is the presence of pores or the vacuous spaces that are related to the osteocyte lacunae, osteonal canals, and analogous non-mineralized architectural features of bone (Zioupos et al., 2008).

The ASTM method showed a direct correlation between the porosity percent and water absorption. The apparent porosity calculated with ASTM compared to the relation with the total porosity (Pt) showed that the pore interconnectivity (pi) is high. Finally, total bone volume is the combined volume of solids and pores, which may contain air or water, or both. As a result, the apparent density is lower than or equal to (in the absence of porosity) the real density (ASTM C20-00, 2015). These results are consistent since the total bone volume (BV/TV) is the combined volume of solids and pores, which may contain air or water, or both. Therefore, as a result, the apparent density is less than or equal (in the absence of porosity) to the real density. The real density of the bone is low compared to the real density of commercial HA (2.83 g/cm^3). It is important to know the density of the bone graft to be used, as this affects the interaction of the material and the tissue (Mbarki, 2017).

3.1.3. Mechanical properties

In Figure 4, it is possible to compare the E (Young's module), H (hardness), and hf (maximum indentation depth after discharge) results in the four PPM sections. The penetration depth-time and load-displacement curves were studied in detail, taking into account the initial contact on the surface, as well as pop-in and viscoelastic creep time effect. A total of 10 indentations were made per sample. Creep period was useful to produce an initial unloading slope free of reverse plasticity (Oliver and Pharr, 1992).

The results indicate that a statistically significant difference ($P < 0.05$) exists with a 95% confidence level comparing the mean of the E (GPa) between the surfaces and transversal sections. On the other hand, there is no statistically significant difference in the means E (GPa) nor between SS and IS, nor CO and SG. Morphology clearly shows the difference between the surfaces and cross sections (see Figure 2), which refers to anisotropy of the bone reflected by the differences in mechanical properties (See Figure 4-a) as is also reported in other studies (Guidoni et al., 2010; Sobota et al., 2017). The CO and SG (cross sections) bone transversal sections are more compact (see Figures 2g and h) due to the wall that forms the concentric lamellae, explaining the higher modulus obtained in these transversal sections. Although there are many models of nanoscale bone deformation mechanisms associated with their hierarchical level, they are still not well understood (Guidoni et al., 2010).

Conversely, no difference was detected in the mean hardness value between the different sections. Hardness is quite closely related to yield stress in plastic materials such as metals, but the hardness of biological tissues like bone is less well-defined (Moreau et al., 2007). However, bone is more prone to behave like a brittle material, and hardness is highly influenced by the densifications and cracking beneath the indenter. A deeper study is necessary to understand the behavior of the hardness found in present study.

3.2. Chemical analysis

The chemical composition of the bone was determined by different techniques. These combined analyzes allowed to determine the chemical composition and crystalline structure of the mineral phases.

3.2.1. Thermal analysis

TGA curves of the PPM and HA samples are shown in Figure 5. The DTGA curve shows that the first weight loss occurred between 40 °C and 180 °C (peak at 80 °C) which is due to the dehydration of bone. Another weight loss occurs between 200 °C and 420 °C (peak at 335 °C) and between 420 °C and 620 °C (peak at 474 °C). They are due to the combustion of the organic components of bone such as collagen and other residual organic components associated with this molecule and involves the additional decomposition of degraded solid substances as reported by other authors (Figueiredo et al., 2011; Raja et al., 2009). The residual mass, a measure of the inorganic contents, showed that the mineral content of hard palate bone was about 59%. Taking into account that the initial mass loss, a measure of water content, is about 7.4%, it can be concluded that the organic content is about 35%. These results show that despite the bone cleaning process, the organic components associated with collagen are still present. In contrast, HA has a moisture content of approximately 5.6% and obviously does not show a thermal decomposition associated with the organic component. These results are consistent with those reported by Figueiredo et al. (2011) who compared human, porcine, and bovine bone. These showed little variations of the weight (%) of the main constituents of human and pig bones, regardless of the donor site.

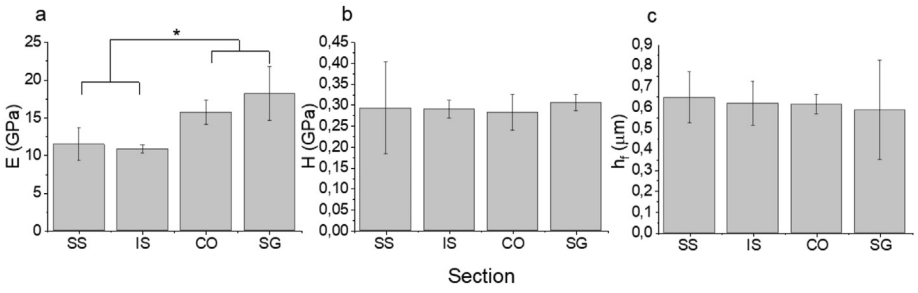

Figure 4. Summary of nanoindentation results. * Significant difference ($P < 0.05$). Data were analyzed by analysis of ANOVA. Mean ± S.D.,n = 7.

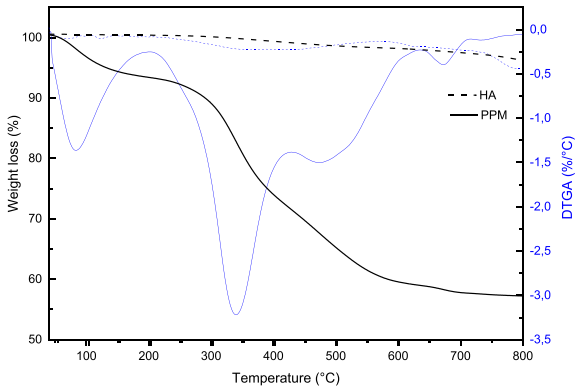

Figure 5. Thermogravimetric analysis of PPM (straight lines) and HA (dash lines).

3.2.2. Elemental analyses

The chemical composition of the inorganic phase found in the TGA was analyzed by other techniques as shown below. Table 2 lists the main elements found in PPM and HA by XRF analysis. The highest percentage of ions are Ca and P with small amounts of Mg and Fe in both samples. Na, S, Si, K, Cl, and Zn were found only in the bone samples. As reported in the literature, all the bone ions play a vital role in the biological reactions associated with the bone metabolism (Figueiredo et al., 2010; Wu et al., 2014). In atomic weight, the Ca/P molar ratio was 1.02 and 1.62 for bone and HA respectively. The results by EDS also showed that PPM has a low Ca/P molar ratio, between 0.931 and 1.324, in all four sections (see Figure 6). In this study, the PPM Ca/P molar ratio is low compared to the HA because the specimen was young at time of death (Gedrange et al., 2001), as demonstrated in the morphology section. When comparing bone to commercial HA, many studies have reported that mature bone has a Ca/P ratio of approximately 1.67, which is close to ideal stoichiometry (Boskey, 2003; Legros et al., 1987). The reports in the literature show that the crystal size, Ca/P molar ratio, and CO_3^{2-} ion content of cortical bone increase with age because the initial phase in calcified tissues is not HA, but it needs a precursor with a low Ca/P ratio to develop HA. This precursor can be an amorphous calcium phosphate (ACP) or octacalcium phosphate (OCP) phase (Boskey, 2003; Legros et al., 1987). However, natural apatite is often not stoichiometric and is not composed by a single phase.

Table 2. Results of elemental analysis of PPM and HA by XRF (% mass).

Element	Elemental content (% mass)	
	XRF*	
	PPM	HA
Ca	24.38	39.92
P	18.68	19.12
Na	1.06	-
Mg	0.359	0.186
S	0.39	-
K	0.041	-
Cl	0.022	-
Mn	-	0.004
Al	-	0.025
Fe	0.017	0.01
Si	0.066	-
Zn	0.017	-
Ca/P	1.02	1.62

* Elements contents were determined by stoichiometry relationships of the oxidized compounds found by XRF.

The SEM/EDS mapping analysis shows that the distribution of calcium and phosphate atoms were uniformly distributed over the entire surface in the four sections (see Figure 6). A high concentration of Ca was registered at all points due to the rate of bone formation and bone resorption during the remodeling process, where Ca plays an important role in the formation of new bone crystals as reported in the literature (Glimcher, 1998). It is important to note that some studies confirm that bone remodeling cycle in pigs is histologically closer to that of the human than other species such as rats or mice (Litten-Brown et al., 2010).

Comparing the results obtained by XRF and EDS, in XRF could detect major, minor, and trace levels of an element important for the bone characterization, while EDS is limited to major and minor elemental concentrations and it is a punctual technique, but EDS analysis allowed us to see the distribution of calcium and phosphorous, along the surface of the bone.

3.2.3. FTIR analysis

FTIR was used to identify the main functional groups of the inorganic and organic compounds that were found in the TGA analysis. Figure 7 shows the FTIR results in which it is possible to identify the spectral differences between PPM and HA, and the presence of carbonate (CO_3^{2-}) and phosphate (PO_4^{3-}) functional groups in the bone sample (Mamede et al., 2018). The wide shape of the bands ν_3 PO_4^{3-} (1200-900 cm^{-1}) in PPM indicates a low crystallinity (Querido et al., 2013). The band ν_1 PO_4^{3-} (980-940 cm^{-1}) appeared as a discrete shoulder in the band ν_3 PO_4^{3-}, and the band ν_4 PO_4^{3-} (650-500 cm^{-1}) was partially resolved in two large peaks in both PPM and HA (Querido et al., 2013).

FTIR analysis is important to determine the presence of bone impurities as HPO_4 and CO_3^{2-}, which substitute in HA some lattice positions (Boskey and Mendelsohn, 2005). Carbonate is the most abundant substitution in bone mineral. FTIR results showed the presence of CO, according to its crystal position is designated as "type A'' (OH^-) or "type B'' (PO_4^{3-}), the latter being the most frequent in natural bone. With an increase in the carbonate content, there is a decrease in crystallinity, therefore, the solubility of calcium phosphate increases, improving its biodegradability (Figueiredo et al., 2010). The ν_3CO_3 (carbonate type B substitution) and the ν_2CO_3 (carbonate type A substitution) are attributed to typical bands of the HA at 1600-1350 cm^{-1} and 890-850 cm^{-1}, respectively. Type A carbonate is present in HA in smaller amounts compared to type B, as a shoulder around 876.5 cm^{-1}, while type B is observed as a double band at 1451.1/1411.6 cm^{-1} (Figure 6) (Figueiredo et al., 2010). In PPM these bands are not clear, and the ν_3 CO_3^{2-} band is overlaid by amides belonging to the organic phase of bone (Alvarez-Lloret et al., 2006).

The FTIR spectra showed the main characteristics of type I collagen in PPM (the predominant protein component of bone) with absorption bands of amide I at ~1632.4cm^{-1}, as results from the stretching vibration of the peptide carbonyl group (–C=O); the amide II at ~1548.5 cm^{-1}, and a set of three weaker bands that represent amide III vibration modes centered at ~1242.8 cm^{-1} (Figueiredo et al., 2010; Vidal and Mello, 2011). The peak of –OH (3279.68 cm^{-1}) was observed in the PPM; FTIR spectra associated to water content in the sample registered in TGA as 7.4 % also as reported in the literature (Drouet, 2013; Mamede et al., 2018). For this research, FTIR- ATR spectroscopy was suitable for biological tissue analyses because it is non-destructive, is insensitive to water content, requires little or no sample preparation and it allowed comparisons between the bone samples and HA.

3.2.4. XRD analysis

In the X-ray diffraction profiles, the level of certainty of the identification in each bone was based on the relationship between the number of paired peaks and the possible total peaks according to the X'Pert HighScore Plus software. The main phases in HA were apatite ($C_{0.01}$ $H_{1.3}$ $Ca_5O_{13.33}$ P_3) and apatite ((CaOH) $H_1Ca_5O_{13}P_3$) with a match of 90% and 7.5% respectively. In contrast, PPM has a mixture of Calcium Vi ($Ca_{10.681}$), Octacalcium Dihydrogen Hexakis (phosphate (V))

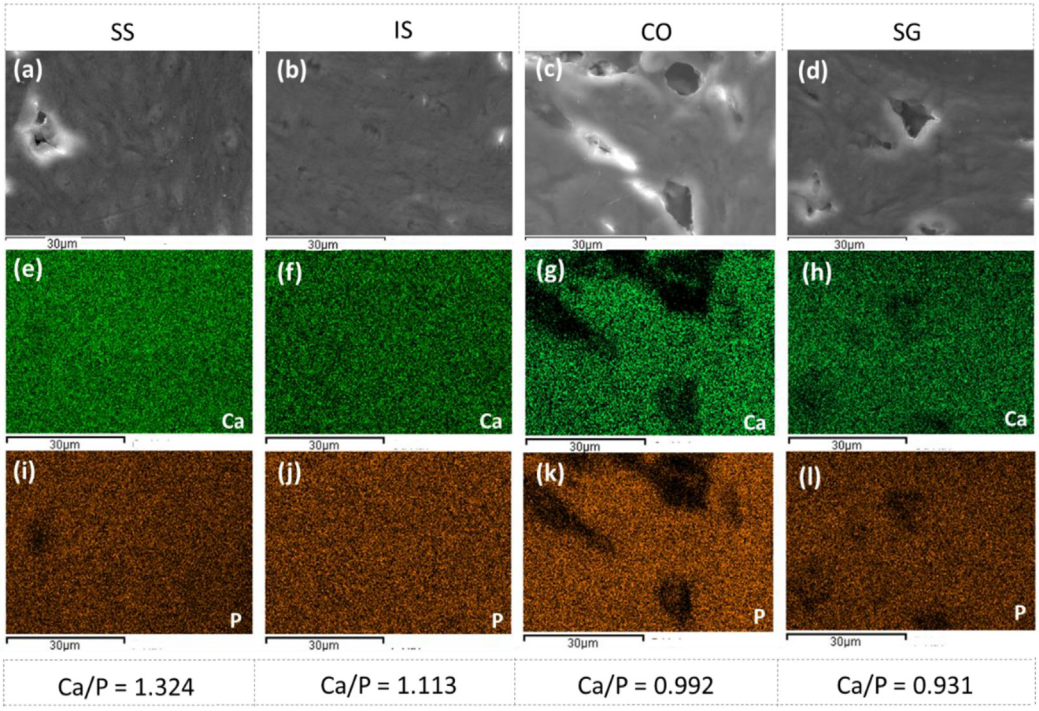

Figure 6. SEM-EDS mapping of the PPM in the four sections. a) SS section; b) IS section; c) CO section; and d) SG section.

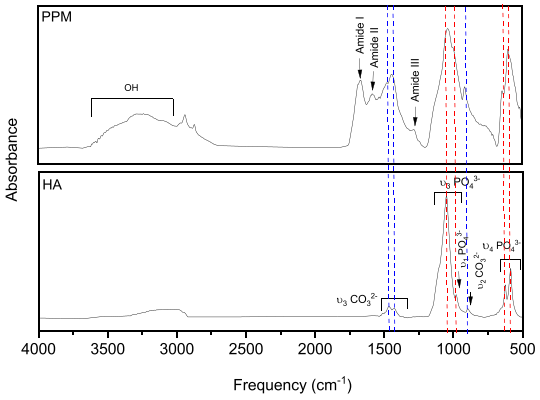

Figure 7. FTIR spectrums of PPM and HA.

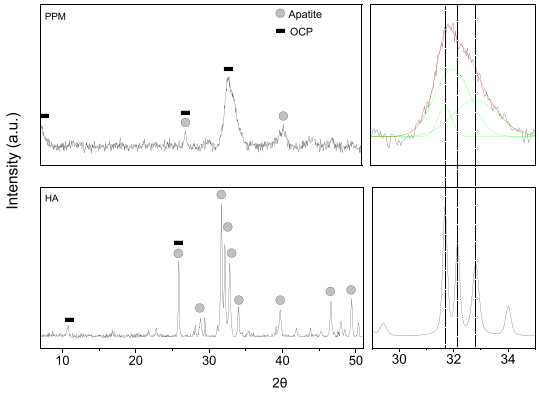

Figure 8. X-ray diffraction patterns of PPM and HA for comparison purposes.

Pentahydrate ($H_{12}Ca_8O_{29}P_6$) (OCP), and apatite (CaOH), where OCP is the predominant phase. As reported in the literature, the OCP phototype is the main inorganic phase in the human body and has been shown to be structurally related to hydroxyapatite (Mathew et al., 1988) having a key role in the bone growth process.

The main HA peaks that indicate apatite phases are 25.86°, 28.73°, 31.6°, 32.14°, 32.8°, 34.01°, 39.67°, 46.57° and 49.41°, which correspond respectively to (0 0 2), (1 0 2), (2 1 1), (1 1 2), (3 0 0), (2 0 2), (3 1 0), (2 2 2) and (2 1 3) diffraction planes (Aguiar et al., 2018; Shahabi et al., 2014). On the other hand, PPM peaks corresponding to the apatite phase are 25.76° and 39.78°, corresponding to the (0 0 2) and (3 1 0) diffraction planes. The PPM diffraction presented broad peaks indicating characteristic bands of calcium phosphate structures between 31° and 33° for 2θ angles (Aguiar et al., 2018). The OCP phase is identified at 25.86° and in the PPM sample at 4.7° and 33.6° (Davies et al., 2014; Morimoto et al., 2012). This is a less crystalline phase than HA, thanks to the water molecules linked to its structure (Davies et al., 2014; Mathew et al., 1988).

The profile of mineral crystals in bone tissue is broad mainly due to low crystallinity compared to materials with high crystallinity such as the HA that have sharper peaks in (2 1 1), (1 1 2), and (3 0 0) planes (Boskey, 2003; Tadano and Giri, 2011), as observed in Figure 8. These broad bands are attributable to the small size of the bone mineral crystals as reported in Table 3 and to the inclusion of vacancies such as Mg^{2+}, Na^{2+}, K^{+}, CO_3^{2-}, HPO_4^{2-}, etc. in the HA crystal lattice. The presence of these ions was demonstrated in FRX and FTIR analyses. Using a Gaussian mathematical function, it was possible to fit the diffracted bone intensity profile near the peaks of HA with an $R^2 = 0.980$. The deconvolution is shown in Figure 8, and Table 3 reports the three main planes after this deconvolution in PPM compared with HA. It is important to emphasize that the TGA and FTIR analysis revealed an organic phase in PPM. This content of organic PPM can complicate the physical-chemical analysis using the XRD technique, hiding some peaks.

Table 3. Planes by XRD after the deconvolution in PPM compared with the HA.

Plane	Profile of mineral crystals			Apparent crystal size	
	211	112	300	002	(τ) nm
PPM	31.71	31.91	32.72	25.75	26.18
HA	31.68	32.14	32.81	25.81	54.36

4. Conclusions

The information obtained in this study provided morphological, chemical, and physical characteristics of hard palate bone (specifically the maxillary palatine process), which have not yet been clearly correlated in the literature. The physical characterizations showed us that the analyzed bone was from a young individual. Morphological analysis did not show the presence of fully formed bone structures (secondary osteons). Additionally, Young's modulus analysis showed different microstructural characteristics in the morphology of the surfaces and the cross sections, confirming the bone anisotropy. On the other hand, the morphology, density and porosity analysis determined that the region of the evaluated palate had characteristics of compact bone.

Thermogravimetric analysis and infrared spectroscopy evidenced the presence of an organic and an inorganic phase in the bone. Elemental analysis showed that bone is mainly composed of calcium and phosphorus. The Ca/P ratio varies depending on the area where the analysis is performed and is associated with the bone remodeling process. The diffractograms, on the other hand, showed that the bone has different phases of calcium phosphates and a lower crystallinity compared to HA. This low crystallinity is associated with the other ions found with XRFs, which affect the shape and size of the inorganic crystal.

The limitations of this study must also be considered. First, the study was done on a relatively young animal model. The maturation and aging process of the bone was therefore considered. Another limitation is the low availability of information in the references on the quality of the bone sample to be explored. Therefore, this research shows different techniques to evaluate and characterize some properties of bone and their correlations among them, treating the hard palate bone as a material. The techniques presented in this research can be used as a diagnostic tool for the determination of bone quality in dry bones of different animals. When the model animal is chosen, it is important to indicate the immature or mature bone stage. The composition, density, porosity, morphology, and mechanical properties depend on the model age and skeletal growth. The results show that natural pig bone differs from commercial HA in many aspects, like chemical composition, and affects the stoichiometry and phase's content, crystallinity, crystal size, and mechanical properties.

Declarations

Author contribution statement

A. Cañas-Gutiérrez: Conceived and designed the experiments; Performed the experiments; Analyzed and interpreted the data; Wrote the paper.

D. Arboleda-Toro: Performed the experiments; Contributed reagents, materials, analysis tools or data; Wrote the paper.

T. Monsalve-Vargas: Contributed reagents, materials, analysis tools or data.

B. Castro-Herazo: Conceived and designed the experiments; Contributed reagents, materials, analysis tools or data.

J.M. Meza-Meza: Conceived and designed the experiments; Contributed reagents, materials, analysis tools or data; Wrote the paper.

Funding statement

This work was supported by Universidad Pontificia Bolivariana and Departamento Administrativo de Ciencia, Tecnología e Innovación (COLCIENCIAS) (727-2015).

Data availability statement

No data was used for the research described in the article.

Declaration of interests statement

The authors declare no conflict of interest.

Additional information

No additional information is available for this paper.

References

Aerssens, J., Boonen, S., Lowet, G., Dequeker, J., 1998. Interspecies differences in bone composition, density, and quality: potential implications for in vivo bone research. Endocrinology 139, 663–670.

Aguiar, H., Chiussi, S., López-Álvarez, M., et al., 2018. Structural characterization of bioceramics and mineralized tissues based on Raman and XRD techniques. Ceram. Int. 44, 495–504.

Alverez-Lloret, P., Rodriguez-Navarro, a. B., Romanek, C.S., et al., 2006. Quantitative analysis of bone mineral using Ftir. Macla 6, 45–47.

ASTM C20-00, 2015. Standard Test Methods for Apparent Porosity , Water Absorption , Apparent Specific Gravity , and Bulk Density of Burned Refractory Brick and Shapes by Boiling Water.

Boskey, A., 2003. Bone mineral crystal Size, 14, pp. 16–21.

Boskey, A., Mendelsohn, R., 2005. Infrared analysis of bone in health and disease. J. Biomed. Opt. 10, 31102.

Boyde, A., Hobdell, M.H., 1968. Scanning electron microscopy of lamellar bone. Z. für Zellforsch. Mikrosk. Anat. 93, 213–231.

Boyde, A., Jones, S., 1998. Aspects of Anatomy and Development of Bone: the Nm, μm and Mm Hierarchy.

Bromage, T.G., Goldman, H.M., McFarlin, S.C., et al., 2003. Circularly polarized light standards for investigations of collagen fiber orientation in bone. Anat. Rec. Part B New Anat 274B, 157–168.

Bush, M.A., Miller, R.G., Norrlander, A.L., Bush, P.J., 2008. Analytical survey of restorative resins by SEM/EDS and XRF: databases for forensic purposes. J. Forensic Sci. 53, 419–425.

Davies, E., Muller, K.H., Wong, W.C., et al., 2014. Citrate bridges between mineral platelets in bone. Proc. Natl. Acad. Sci. Unit. States Am. 111, E1354–E1363.

Drouet, C., 2013. Apatite formation: why it may not work as planned, and how to conclusively identify apatite compounds. BioMed Res. Int. 2013, 12 pages.

Dumont, E., 2010. Bone density and the lightweight skeletons of birds. Proc. R Soc. B Biol. Sci. 277, 2193–2198.

Figueiredo, M., Fernando, A., Martins, G., et al., 2010. Effect of the calcination temperature on the composition and microstructure of hydroxyapatite derived from human and animal bone. Ceram. Int. 36, 2383–2393.

Figueiredo, M., Cunha, S., Martins, G., et al., 2011. Influence of hydrochloric acid concentration on the demineralization of cortical bone. Chem. Eng. Res. Des. 89, 116–124.

Gedrange, T., Köbel, C., Harzer, W., 2001. Hard Palate Deformation in an Animal Model Following Quasi-Static Loading to Stimulate that of Orthodontic anchorage Implants, 23, pp. 349–354.

Georgiadis, M., Müller, R., Schneider, P., 2016. Techniques to assess bone ultrastructure organization: orientation and arrangement of mineralized collagen fibrils. J. R. Soc. Interface 13, 1–26.

Gibson, V.A., Stover, S.M., Gibeling, J.C., et al., 2006. Osteonal effects on elastic modulus and fatigue life in equine bone. J. Biomech. 39, 217–225.

Glimcher, M.J., 1998. The nature of the mineral phase in bone: biological and clinical implications. In: Metabolic Bone Disease and Clinically Related Disorders. Woodhead Publishing Limited, pp. 23–50.

Gracco, A., Lombardo, L., Cozzani, M., Siciliani, G., 2008. Quantitative cone-beam computed tomography evaluation of palatal bone thickness for orthodontic miniscrew placement. Am. J. Orthod. Dentofacial Orthop. 134, 361–369.

Guidoni, G., Swain, M., Jäger, I., 2010. Nanoindentation of wet and dry compact bone: influence of environment and indenter tip geometry on the indentation modulus. Philos. Mag. A 90, 553–565.

Hafsteinsdóttir, E.G., White, D.A., Gore, D.B., 2013. Effects of freeze e thaw cycling on metal-phosphate formation and stability in single and multi-metal systems. Environ. Pollut. 175, 168–177.

Hoffler, C.E., 2005. An application of nanoindentation technique to measure bone tissue lamellae properties. J. Biomech. Eng. 127, 1046.

Huang, J., Tianc, B., Chua, F., et al., 2015. Rapid maxillary expansion in alveolar cleft repaired with a tissue-engineered bone in a canine model. J. Mech. Behav. Biomed. Mater. 48, 86–99.

Inui, A., Itamoto, K., Takuma, T., et al., 2004. Age-related changes of bone mineral density and microarchitecture in miniature pigs. J. Vet. Med. Sci. 66, 599–609.

Legros, R., Balmain, N., Bonel, G., 1987. Age-related changes in mineral of rat and bovine cortical bone. Calcif. Tissue Int. 41, 137–144.

Litten-Brown, J.C., Corson, A.M., Clarke, L., 2010. Porcine models for the metabolic syndrome , digestive and bone disorders : a general overview. Animal 4, 899–920.

Liu, J., Miao, X., 2005. Porous alumina ceramics prepared by slurry infiltration of expanded polystyrene beads. J. Mater. Sci. 40, 6145–6150.

Malluche, H.H., Porter, D.S., Monier-Faugere, M.-C., et al., 2012. Differences in bone quality in low- and high-turnover renal osteodystrophy. J. Am. Soc. Nephrol. 23, 525–532.

Mamede, A.P., Vassalo, A.R., Cunha, E., et al., 2018. Biomaterials from human bone-probing organic fraction removal by chemical and enzymatic methods. RSC Adv. 8, 27260–27267.
Martiniaková, M., Omelka, R., Grosskopf, B., et al., 2008. Sex-related variation in compact bone microstructure of the femoral diaphysis in juvenile rabbits. Acta Vet. Scand. 50, 1–6.
Matassi, F., Nistri, L., Paez, D.C., Innocenti, M., 2011. New biomaterials for bone regeneration. Clin Cases Miner Bone Metab 8, 21–24.
Mathew, M., Brown, W.E., Schroeder, L.W., Dickens, B., 1988. Crystal structure of octacalcium bis(hydrogenphosphate) tetrakis(phosphate)pentahydrate, Ca8(HP04) 2(PO4)4.5H2O. J. Crystallogr. Spectrosc. Res. 18, 235–250.
Mbarki, M., et al., 2017. Hydroxyapatite bioceramic with large porosity. Mater. Sci. Eng. C 76, 985–990.
Melsen, B., 1975. Palatal growth studied on human autopsy material. A histologic microradiographic study. Am. J. Orthod. 68, 42–54.
Montenegro, M.A., Rojas, M., 2005. Aspectos Moleculares en la Formación de la Cara y del Paladar. Int. J. Morphol. 23, 185–194.
Moreau, J.L., Caccamese, J.F., Coletti, D.P., et al., 2007. Tissue engineering solutions for cleft palates. J. Oral Maxillofac. Surg. 65, 2503–2511.
Morimoto, S., Anada, T., Honda, Y., Suzuki, O., 2012. Comparative study on in vitro biocompatibility of synthetic octacalcium phosphate and calcium phosphate ceramics used clinically. Biomed. Mater. 7.
Oliver, W.C., Pharr, G.M., 1992. An improved technique for determining hardness and elastic modulus using load and displacement sensing indentation experiments. Mater. Res. Soc. 7, 1564–1583.
Pazzaglia, U.E., Congiu, T., Marchese, M., et al., 2012. Morphometry and patterns of lamellar bone in human Haversian systems. Anat. Rec. 295, 1421–1429.
Pyszko, M., Paral, V., Kyllar, M., 2013. Thickness of the substantia compacta of porcine long bones. Vet. Med. (Prague) 58, 543–552.
Querido, W., Rossi, A.L., Campos, A.P.C., et al., 2013. Does crystallinity of extracted bone mineral increase over storage time? Mater. Res. 16, 970–974.
Raja, S., Thomas, P.S., Stuart, B.H., et al., 2009. The estimation of pig bone age for forensic application using thermogravimetric analysis. J. Therm. Anal. Calorim. 98, 173–176.
Reznikov, N., Bilton, M., Lari, L., et al., 2018. Fractal-like hierarchical organization of bone begins at the nanoscale. Science (80-) 360, 1–10.
Shah, S., Garritano, F.G., 2015. Pediatric oral anatomy. Operat. Tech. Otolaryngol. Head Neck Surg. 26, 2–7.
Shah, F.A., Ruscsák, K., Palmquist, A., 2019. 50 Years of scanning electron microscopy of bone—a comprehensive overview of the important discoveries made and insights gained into bone material properties in health, disease, and taphonomy. Bone Res. 7, 15.
Shahabi, S., Najafi, F., Majdabadi, A., et al., 2014. Effect of gamma irradiation on structural and biological properties of a PLGA-PEG-hydroxyapatite composite. Sci. World J. 2014.
Sobota, M., Jurczyk, S., Smola-dmochowska, A., et al., 2017. Mechanical characterization via nanoindentation of the woven bone developed during bone transport. J. Mech. Behav. Biomed. Mater. 74, 236–244.
Starup-Linde, J., Lykkeboe, S., Gregersen, S., et al., 2016. Differences in biochemical bone markers by diabetes type and the impact of glucose. Bone 83, 149–155.
Sun, L., Wang, J., Liu, H., et al., 2017. A comprehensive study of palate development in miniature pig. Anat. Rec. 300, 1409–1419.
Tadano, S., Giri, B., 2011. X-ray diffraction as a promising tool to characterize bone nanocomposites. Sci. Technol. Adv. Mater. 12, 1–11.
Tenorio Estrada, J.K., 2017. Relación entre la maduración ósea y la osificación de la sutura palatina media en pacientes de 10 - 20 años . 2014-2016.
Vidal, B.D.C., Mello, M.L.S., 2011. Collagen type I amide I band infrared spectroscopy. Micron 42, 283–289.
Watson, P.J., Fitton, L.C., Meloro, C., et al., 2018. Mechanical adaptation of trabecular bone morphology in the mammalian mandible. Sci. Rep. 8, 1–12.
Wu, Z., Ovaert, T.C., Niebur, G.L., 2012. Viscoelastic Properties of Human Cortical Bone Tissue Depend on Gender and Elastic Modulus, 30, pp. 693–699.
Wu, S., Liu, X., Yeung, K.W.K., et al., 2014. Biomimetic porous scaffolds for bone tissue engineering. Mater. Sci. Eng. R 80, 1–36.
Zioupos, P., Cook, R.B., Hutchinson, J.R., 2008. Some basic relationships between density values in cancellous and cortical bone. J. Biomech. 41, 1961–1968.